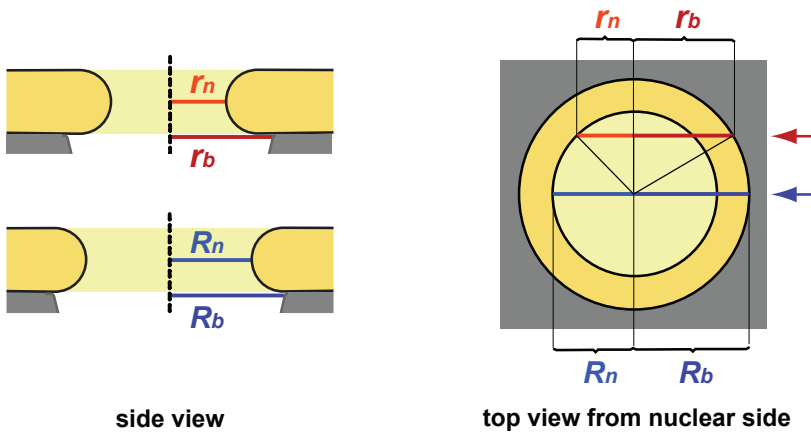**Supplementary Figure S1. HEZs in HeLa cells prior to and after PV-infection resemble HEZs in terminally differentiated cells. (A)** Regions of close contact between NE and heterochromatin (hc), and between NE and the granular components of the nucleolus (no) in non-infected HeLa cells, showing NPC-associated exclusion zones of trapezoid-like section planes, or with seemingly parabolic or hyperbolic contours. Occurrence of such HEZs reveals that not only heterochromatin, but also the granular material of the nucleolus, thought to mainly represent pre-ribosomal particles in various stages of maturation [see supplementary reference S1], is excluded from a zone in front of at least a subgroup of NPCs in these cells. In general, however, only a small part of the NE in a proliferating cultured cell in interphase is intimately connected to such local accumulations of heterochromatin or nucleolar material. Moreover, NPCs appear to occur rather sparsely in such contact regions[S2-4]. When evaluating randomly chosen sections of interphase cells, originating from two HeLa cell cultures, chronologically apart from each other by >50 cell passages, we found that of all perpendicularly sectioned NPCs (n_{total}=390; selection criteria according to Supplementary Figure S2) only 5.2-6.4% (n_{total}=23) were facing clusters of heterochromatic or nucleolar material. Most of these NPCs exhibited an HEZ of the trapezoid-type (87%, n=20) or of long channel-like appearance (4.3%, n=1), whilst the borderlines of two potential HEZs were indistinct. Interestingly, *S. cerevisiae* NPCs in direct contact with the nucleolus appear to lack these exclusion zones but appear to be functional in rRNA export[S5] nonetheless. Remarkably, GFP-tagged Mlp1p and Mlp2p, the Tpr homologs in *S. cerevisiae*, do not attach to all NPCs but are largely absent from those next to the nucleolus[S6]. In contrast, the NPCs of another unicellular organism, *Dictyostelium discoideum*, are outfitted with clearance zones when intimately connected to the nucleolus[S7, S8], in line with *Dictyostelium* Tpr being found at essentially all NPCs in this organism (our unpublished data). Why NPC-associated exclusion zones are present in the one case but dispensable in the other is unknown. Further, the borderlines of such zones are also respected in pathological situations, such as when highly condensed chromatin amasses at the nuclear periphery of vertebrate Lmna-/- cells[S9] and in cells with homozygous mutations in the lamin B receptor[S10]. Moreover, homozygous deletion of the murine *Aladin* gene, which encodes a nucleoporin of the NPC proper with a role in nuclear protein import[S11-14], does not prevent HEZ formation either[S15]. Bar, 200 nm, same magnification for all images. **(B1-B3)** After PV-infection of HeLa cells, amassments of condensed chromatin contour HEZs of different sizes, with a seemingly temporal order of their predominant occurrence. At 8 h post-infection (pi), the measured lengths of most HEZ sections associated to perpendicularly cross-sectioned NPCs with clear NPC channel walls ranged between 100-150 nm (55%). Larger values were obtained too (4%) but HEZ sections exceeding 200 nm were rare (1%). Shorter section lengths mainly ranged between 60 and 100 nm (39%). At 10-12 h pi, the majority of measured section lengths ranged between 60 and 100 nm (64-68%), often exceeding 80% in cells with a highly distorted nucleus filled by densely packed chromatin, whilst the proportion of very short sections (<60 nm) was similar at all time points (≤2%), applying selection criteria for NPC sections described in (S2). The vast majority of perpendicularly cross-sectioned NPCs with clear-cut NPC channel walls were found associated with such HEZs (95%-98.0%, n=346-358 [10 h pi], 96%-98%, n=310-316 [12 h]; data variations due to differently stringent selection criteria), and only few individual NPCs appeared to lack an HEZ. **(B1)** Representative selection of commonly observed HEZ section shapes of different appearance, here with lengths in the range of 85-165 nm. Also of note, we occasionally found single spherical particles of 18-28 nm diameter within the confinements of such HEZs (arrows in B1 and B2). These particles were located near the HEZ's distal end but not next to or within the NPC core region. It remains unclear whether they
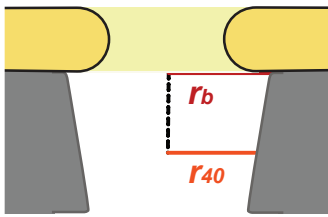
represent RNP particles stalled in transport. **(B2)** Images selected on the basis of nearly identical chord lengths (±1nm) of the perpendicular NPC cross-sections, in order to allow comparison of congruent sectional planes. The HEZ section lengths are ~235 nm and ~140 nm in the left and middle image (both 8 h pi), respectively. In contrast, the HEZ section length in the right image (12 h pi) is ~75 nm, representing a common measurement value for this time point. This image was taken from Fig. 1 B1 (lower arrow) to put the other HEZ section lengths into perspective. **(B3)** Sporadic example of a HeLa cell from 10 h pi in which the infection process appears to have been stalled or aborted at an earlier time point. Many of its NPC-associated HEZ sections have a long, channel- or funnel-like appearance of up to 460 nm in length, next to others of smaller, trapezoid shape. Again other HEZ sections reveal a triangular widening at their distal end. The different shapes of these HEZ sections are highly similar to naturally occurring ones seen in a broad range of normal somatic tissue cells[S16-25] and in various cell-pathological situations[S26-31]. In the present study, such very long HEZs were only rarely observed and it remains unknown whether they represent a transiently visible state at only a small subset of NPCs. Even though very long HEZs often represent long clefts between neighbouring chromosome regions[S3], serial sectioning of cells has also revealed that some of them are longitudinally surrounded by condensed chromatin, indicative that they are of cylindrical shape[e.g. S32, S33; also S30]. Similarly, serial sections of 60-90 nm thickness performed as controls (not shown), revealed the sporadic occurrence of clefts as well as of individual longer HEZs (≥150 nm) surrounded by chromatin also in PV-infected cells. As discussed in the main text, a long tubular HEZ shape suggests the presence of structural elements. Interestingly, a regular arrangement of long thin fibrils, projecting a few hundred nm deep into the nucleus, can be found attached to the distal end of some of the NPC-attached nuclear baskets (NB) in the amphibian oocytes[S34-36] that lack perinuclear heterochromatin[S37]. Whether similar fibrils are part of a scaffold forming the long HEZs in other cell types and which proteins they consist of remain unknown. In somatic cells, a chromatin-specific contribution may be needed to maintain such long channels since they were only found to penetrate chromatin areas but not the nucleolus. Bars, 100 nm (B1), 100 nm (B2), 1 μm (B3); same magnification for all images in B1 and B2, respectively. **(C1, C2)** Spatial and temporal course of changes in nuclear morphology, and chromatin hyper-condensation after PV-infection: **(C1)** Overview images of nuclear cross-sections at different time points post-infection. NE folding was not noted at 5 h pi (upper image). At later time points, nuclei were highly distorted (lower image). However, when measuring the NEs' cross-sectional lengths and approximating the mean NE surface area at 10-12 h pi, we found these mean values to remain similar as compared to control cells, with differences only in the range of -13% to +5% in different measurement and calculation approaches. Moreover, mean NPC densities along the NE cross-sections were similar in infected and non-infected nuclei. Altogether, this indicated that pores were not eliminated within the investigated timeframe. Amassments of condensed chromatin throughout the nucleus were sometimes seen already at 8 h pi (not shown) whereas in other cells the cytopathic effects of PV-infection appeared less advanced or stalled (middle image). In such cells, however, it seemed evident that hyper-condensation starts not only at the NE but also at the periphery (arrow) of the nucleolus (no). In our study, distinct cytopathic phenotypes and degradation of NPC proteins occurred 3-4 h later than in some studies in which other HeLa sublines were used[S38-40]. However, when comparing different infection procedures and using multiplicities of infection (MOI) in the range of 10-50, we found the chronology of the degradation of different NPC proteins relative to each other, and to the occurrence of distinct morphologic phenotypes, to remain unchanged in the HeLa subline used here. Moreover, when comparing the

onset of Nup98 degradation (Fig. 3) at shorter time intervals between 2 h and 5 h pi (not shown), and the occurrence of morphologic phenotypes at later time points, we noted a maximal time lag of only about one hour between different infection protocols. Bar, 500 nm, same magnification for all images. **(C2)** Gradual amassment of condensed chromatin along the NE and towards the nuclear interior. In non-infected control cells (upper row), the amount of peripheral heterochromatin is low in mid-G1 and early S-phase, and only slightly more prominent in late S-phase and G2-phase ([S41]; our unpublished data). An arrow points at an electron-dense NPC-midplane of ~10 nm thickness, characteristic not only for NPCs of chemically fixed HeLa cells but visible also in high-pressure frozen and freeze-substituted mammalian cells[S42]. At 8 h and 12 h pi (lower rows), layers of condensed chromatin masses are often first found laterally distributed along the NE, but later also deep within the nucleus, suggesting that the compaction process spreads from the NE towards the nuclear interior. Bars, 200 nm, same magnification for all images.
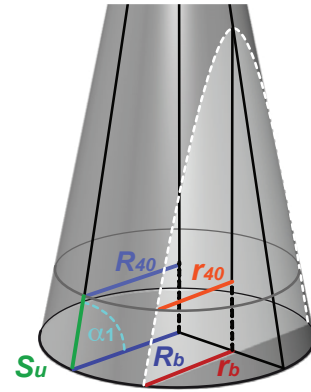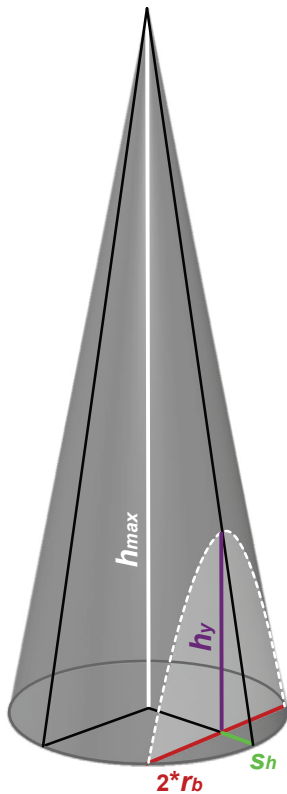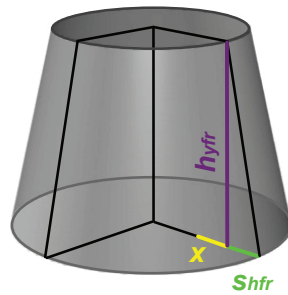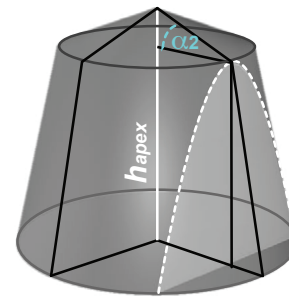
A

side view

top view from nuclear side

B1

B2

C1

C2

C3

C4

R_n = 42 nm

$f(x) = h_{max}/R_b$

$\hat{=} \tan\alpha_2$

$f(x) = h_{yfr}/(s_{hfr}+x)$

R_n = 36 nm

D
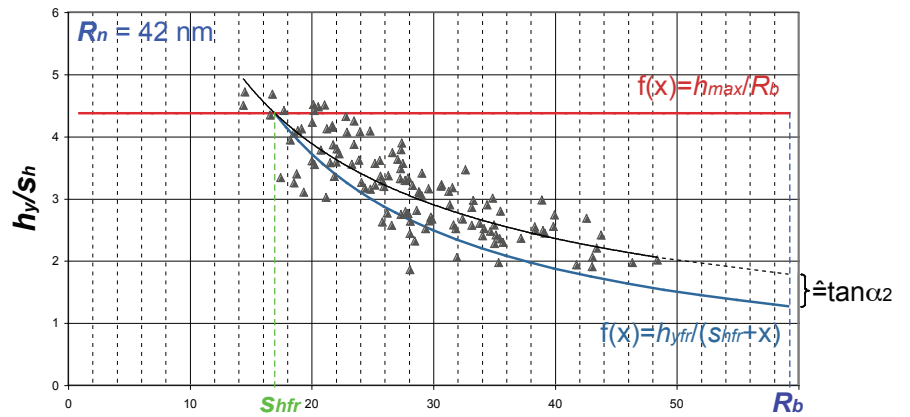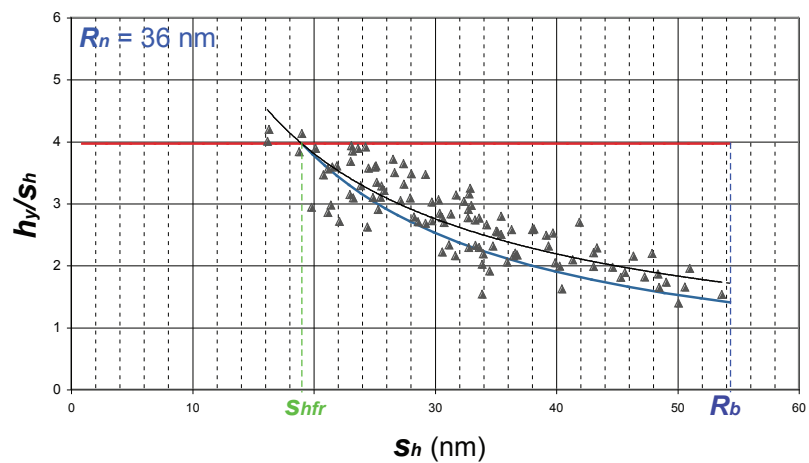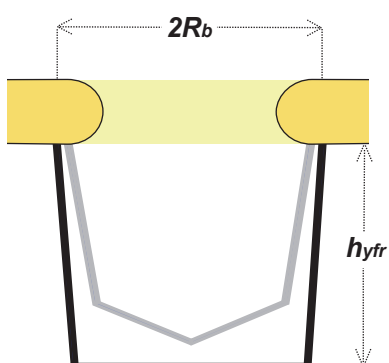
Supplementary Figure S2. Stereometry of NPC-associated HEZs.

To estimate HEZ dimensions without tomographic reconstruction, we applied a stereometric approach by analysing cross-sections of different HEZs. In doing so, two aspects had to be regarded. First, if the modelled mean of a particular type of HEZ was to be a sound estimate of the authentic shape, the corresponding real HEZ would need to be a regularly shaped compartment common to many NPCs. We regarded this condition fulfilled by using HEZ sections from the late stages of PV-infection when HEZ section shapes of rather uniform appearance were found in cells characterized by highly invaginated nuclei and amassments of condensed chromatin. Initial comparisons of measured HEZ section lengths, from different time points after PV-infection and from cells with differently pronounced cytopathic effects, suggested that the short trapezoid section surfaces found at 10 and 12 h pi represented a steady state of a residual HEZ "core" region (before cell disintegration at later time points). Analysis of consecutive sections performed as controls confirmed that these late HEZs were surrounded by condensed chromatin and that their longitudinal axis was usually perpendicular to the NE midplane. These findings, in conjunction with hyperbola- or trapezoid-like contours of the corresponding HEZ sections, led us to approximatively describe the underlying HEZ shape as a cone-like space, instead of as an alternative multi-surface pyramid or a half-ellipsoid. A cone as calculation basis would result in some un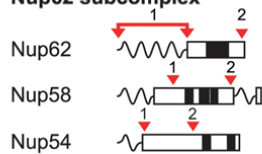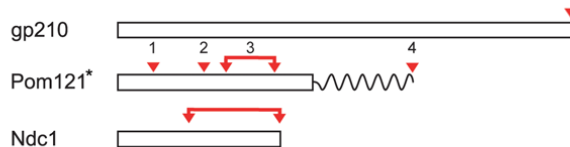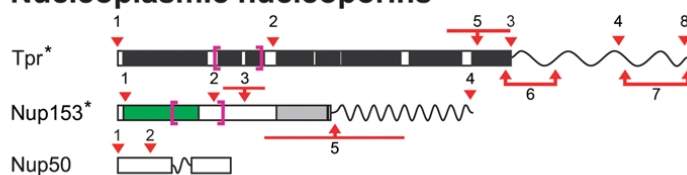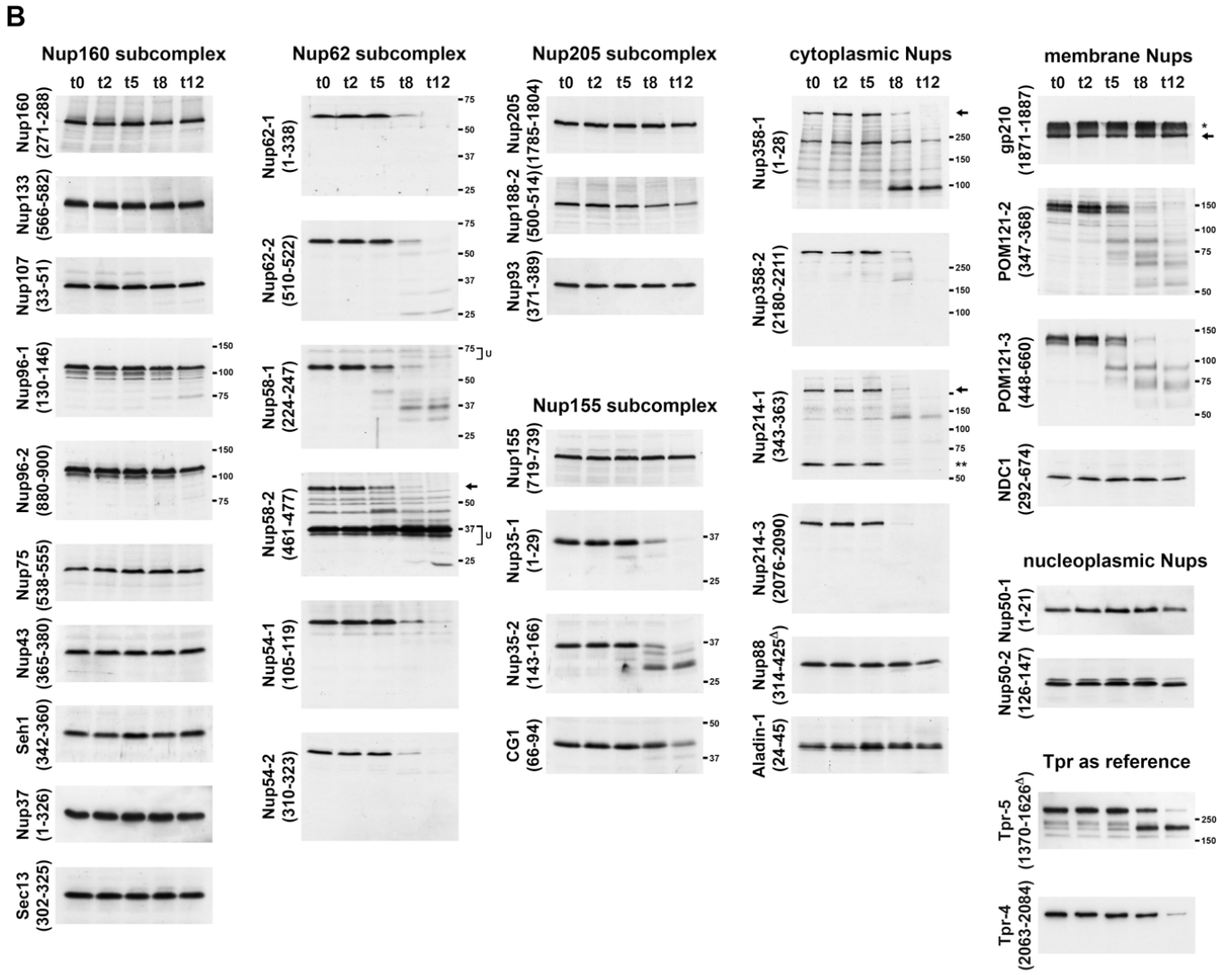derestimation of the HEZ's maximal dimensions if the underlying true shape were a pyramid. However, for a pyramid with octangular base, the mean cone diameter would be only <5% smaller than the long diagonal of the octagon. Secondly, EM micrographs represent a two-dimensional composite of the electron scattering events that occur along the path of the electron beam when crossing a section of finite thickness. They thus reflect the amounts of dense material encountered along the path through such a specimen. This aspect of section thickness can be neglected in post-embedding immuno-EM of the NPC, where the combination of distinct NE walls and NPC-specific gold grain-labelling is generally only observed when the sectioned NE wall is located on the surface[e.g. S43]. However, for stereometry, section thickness has to be taken into account. Since the HEZs to be analyzed were surrounded by densely stained chromatin, and since the HEZ dimensions were in a similar order of magnitude as the thickness of ultrathin sections, this was likely to introduce a systematic error due to difficulties in recognizing the authentic HEZ borderlines, resulting in smaller measurement readings and some further underestimation of actual HEZ dimensions[see also S44, S45]. To reduce this problem, images for size determination were collected from sections of grey to silvery interference colour, equivalent to section thicknesses of about 40-60 nm[S46, S47]. Ample contrast in these thin sections, and uniform chromatin staining throughout the nucleus, was achieved by *en bloc* staining of cells with uranyl acetate, followed by post-staining of sections with lead citrate to enhance chromatin staining intensity[S48, S49]. Furthermore, only those sections whose surface area boundaries appeared distinct were chosen for measurements. This may have resulted in some preference for sections with both surfaces located on opposite sides of the NPC diameter because HEZ section perimeters were expected to often appear less distinct when section slices were from only one side of the NPC diameter. In both cases, however, the error introduced by section thickness would have resulted in an under- but not overestimation of HEZ dimensions. Conscious of the possibility of size underestimation, the following calculations were nonetheless based on the simplification that the micrographs represented depictions of two-dimensional surface planes. **(A)** Normalization of x-axis values for non-diametric perpendicular section planes through the NPC and determination of the radius R_b at the basis of an NPC-associated cone-shaped HEZ: Perpendicular section planes through most NPCs and their associated HEZ did not pass directly through the NPC

center but represented chords that were shorter than the real NPC and HEZ diameters. Consequently, the measured radii (r_n respectively r_b) were smaller than the real radial distance R_n between NPC midaxis [hatched line] and pore wall, and the real radius R_b between midaxis and flanking heterochromatin [grey area]. Since former structure analyses of detergent-extracted *Xenopus* NPCs determined R_n to be 42-43 nm[S50, S51], regarded as representative for other vertebrate NPCs too[S43], R_b could be calculated as the square root of (R_n^2 − r_n^2 + r_b^2), with R_n set to 42 nm. R_{40} at a distance of 40 nm from the inner side of the NE [see (B)] was determined accordingly, using the set value for R_n, and the measurement readings for r_n and r_{40}. Grazing sections of the pore in which r_n was <22.5 nm were not considered[S43]. Sections selected for measuring were regarded as strictly parallel to the central NPC-HEZ axis, even though we could not exclude that some section planes were tilted slightly towards or away from the central cone axis, thus possibly introducing some additional variance of error in calculations of mean values. **(B)** Determination of the angle $\alpha 1$ between the radius R_b and the slant of the cone-shaped HEZ: **(B1)** Having determined R_b and R_{40}, 40 nm apart from each other, **(B2)** the slant segment length S_u could be calculated as the square root of (40^2 + [R_b-R_{40}]^2), allowing to determine $\alpha 1$ according to $\sin\alpha 1 = 40/S_u$. Some few HEZ sections that pointed at a less common three-step cone conformation, with a short shallow slope at the basis, followed by a long steep flank, and another shallow slope towards the top, were not considered for these calculations. **(C)** Trigonometric approximation of the shape at the HEZ's distal end and discrimination between truncated versus pointed cone: **(C1)** The height h_{max} of a HEZ representing a pointed cone with base radius R_b and uniform slant inclination angle $\alpha 1$ would equal R_b*tan$\alpha 1$. Grazing sections parallel to the midaxis of such cones would yield hyperbolic sections (hatched white line), each with a measurable surface height h_y that equals s_h*tan$\alpha 1$, with s_h being the segment height (sagitta) of the base segment with a chord length of 2*r_b and equalling R_b minus the square root of (R_b^2 - r_b^2). For a regular cone with uniform slant angle, the ratio between any h_y and corresponding s_h would equal that of h_{max}/R_b. **(C2)** In contrast, in case of a truncated cone, the maximal value for h_y (= h_{yfr}) would be reached at the transition point between cone flank and cone frustum, corresponding to segment height s_{hfr}. Therefore, at sections with larger segment heights (s_{hfr}+x), the values for h_y/s_h decline, following the hyperbolic equation f(x) = h_{yfr}*(s_{hfr}+x)^-1 [equation 2]. **(C3)** For a cone with oblate apex, where s_{hfr} corresponds to the segment height beyond which the flattened cone top rises with a uniform angle $\alpha 2$, with $\alpha 2$<$\alpha 1$, the corresponding equation would be f(x) = (h_{yfr}+ tan$\alpha 2$*(x-s_{hfr}))*(s_{hfr}+x)^-1 [equation 3]. The value for h_{apex} would then equal h_{yfr}+tan$\alpha 2$*(R_b-s_{hfr}). **(C4)** Plotting h_y/s_h values against s_h values derived from 121 perpendicular HEZ sections from cells at 10-12 h post-PV-infection allowed to approximate the corresponding power trend-line of the equation of type f(x) = a*x^-b [equation 4] and to exclude the occurrence of pointed cones with uniform slant angles. Intersection of this graph with that of equation f(x) = h_{max}/R_b [equation 1] provided an s_{hfr} value beyond which deviation from the linear function occurred. This in turn allowed determining h_{yfr} according to h_{yfr} = s_{hfr}*tan$\alpha 1$. On the other hand, the difference between y values for equations 4 and 2 at x=R_b was equivalent to an approximate value for tan$\alpha 2$. Notably though, the plotted measurements, derived from calculations based on an R_n value of 42 nm (upper diagram) were not uniformly distributed along the x-axis beyond x=s_{hfr} but instead absent proximal to x= R_b. A uniform distribution, however, would have been expected for non-diametric perpendicular NPC/HEZ sections of random section depth and similarly frequent occurrence between s_{hfr} and R_b. In line with this observation, the measurable diameters between all NPC channel walls of HeLa sections at 10-12 h pi were not found to exceed 71 nm, indicative that the actual value for R_n might be smaller than anticipated. Therefore, calculations and
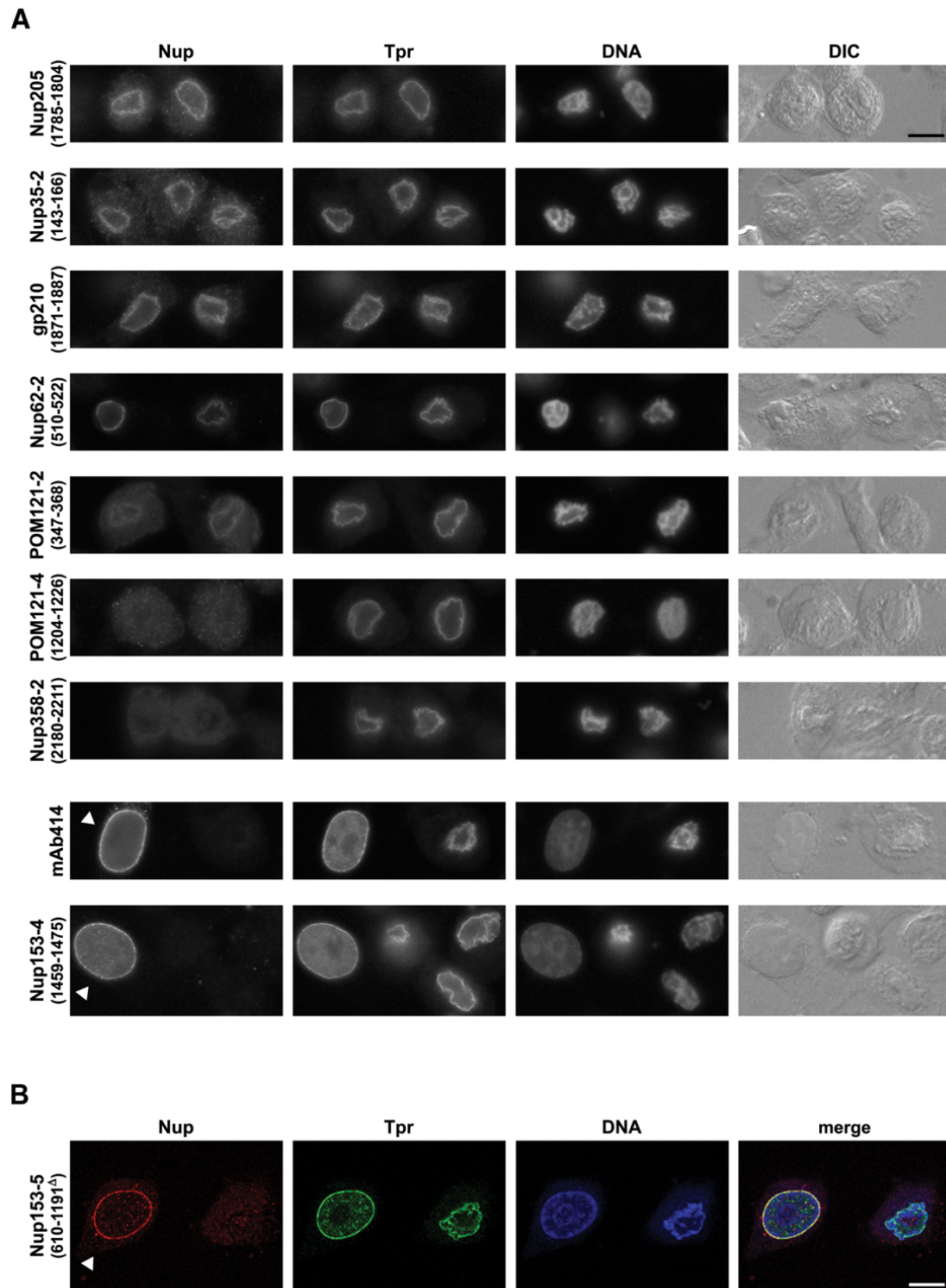
corresponding plot (lower diagram) were also conducted on the basis of a supposed R_n value of 36 nm. This resulted in a mean value for 2xR_b of 109 nm, cone heights h_{yfr} of 76 nm and h_{apex} of 87 nm. Interestingly, pore section diameters of non-infected cells, prepared and analyzed in parallel to the PV-infected ones, were somewhat larger, with mean values for $2*r_n$ exceeding those from the late time points of PV-infection by ~6 nm. How such difference in NPC diameter could be explained architecturally remains unclear. Interestingly though, decrease of pore diameter concomitant to loss of the electron-dense NPC-midplane and to degradation of some NPC core nucleoporins (Supplementary Figure S3) might indicate that such material contributes to maintaining a normal NPC diameter. (**D**) Trigonometric approximation of the dimensions of naturally occurring HEZs (n=16) in non-infected cells, on the basis of an R_n value of 42 nm and starting from HEZ sections of trapezoid-or hyperbola-like contours only. Sections were from cells that had been cultured and processed for EM in parallel to the PV-infected cell cultures used for HEZ stereometry. The schematic depiction of the mean normalized diametric HEZ section (borderlines in black), drawn approximately to scale, reflects mean values for 2xR_b of 129 nm, cone heights h_{yfr} of 105-109 nm and h_{apex} of 106-108 nm, indicative of a truncated cone. Moreover, the mean cone angle α_1 of these naturally occurring HEZs (80°) was steeper than that of the cone-shaped HEZs (borderlines in grey as reference) seen late in PV-infection (77°). The borderlines though at the terminal ends of some of the HEZ sections from non-infected cells appeared less clearly defined than those from PV-infected cells. In combination with a small data set and certain variability in power trend-line approximation for equation 4, this resulted in the range of possible mean h_{yfr} and h_{apex} values. Apart from that, three other HEZ sections from the same specimens, with approximate h_y values of 204, 169, and 152 nm, were not regarded for these calculations. When comparing HEZ sizes one further needs to bear in mind that proteins Nup153 and Tpr in non-infected cells are possibly intact at NPCs outfitted with visible HEZs, whilst Tpr's C-terminal domain and Nup153 are largely degraded in the course of the PV-infection process (see Figure 3). We also note that the mean authentic length of HEZs might be slightly larger in general: Within the ultrathin section, tapering of the cone and concomitant increase of the total chromatin amount along the same electron beam path entails that authentic borderline recognition at the HEZ's distal end can be more error-prone than along its lateral boundaries closer to the HEZ basis. Conservative measurements would thus tend to underestimate especially the HEZ length. This could also result in the calculated angle α_2 to be smaller than in the authentic HEZ late in PV-infection.

A

Cytoplasmic nucleoporins

Nup358

Nup214*

Nup88

Aladin*
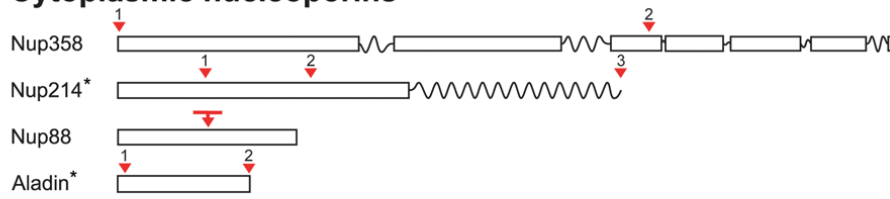
NPC core nucleoporins

Nup160 subcomplex

Nup160

Nup133

Nup96

Nup107

Nup75

Nup43

Seh1

Nup37

Sec13
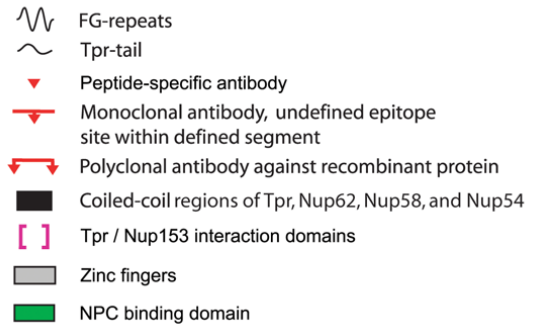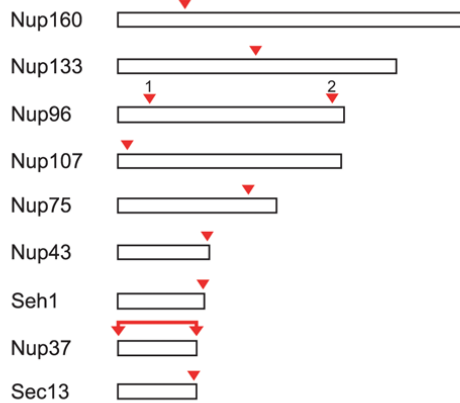
Nup205 subcomplex

Nup205

Nup188*

Nup93

Nup155 subcomplex

Nup155

Nup35

CG1

Nup62 subcomplex

Nup62

Nup58

Nup54
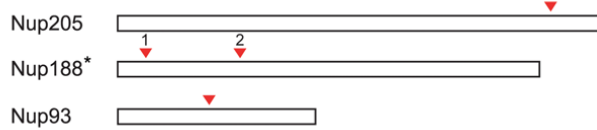
Transmembrane nucleoporins

gp210

Pom121*

Ndc1

Nucleoplasmic nucleoporins

Tpr*

Nup153*

Nup50

Legend:
- ʌʌʌ FG-repeats
- ⌒ Tpr-tail
- ▼ Peptide-specific antibody
- Monoclonal antibody, undefined epitope site within defined segment
- Polyclonal antibody against recombinant protein
- Coiled-coil regions of Tpr, Nup62, Nup58, and Nup54
- [ ] Tpr / Nup153 interaction domains
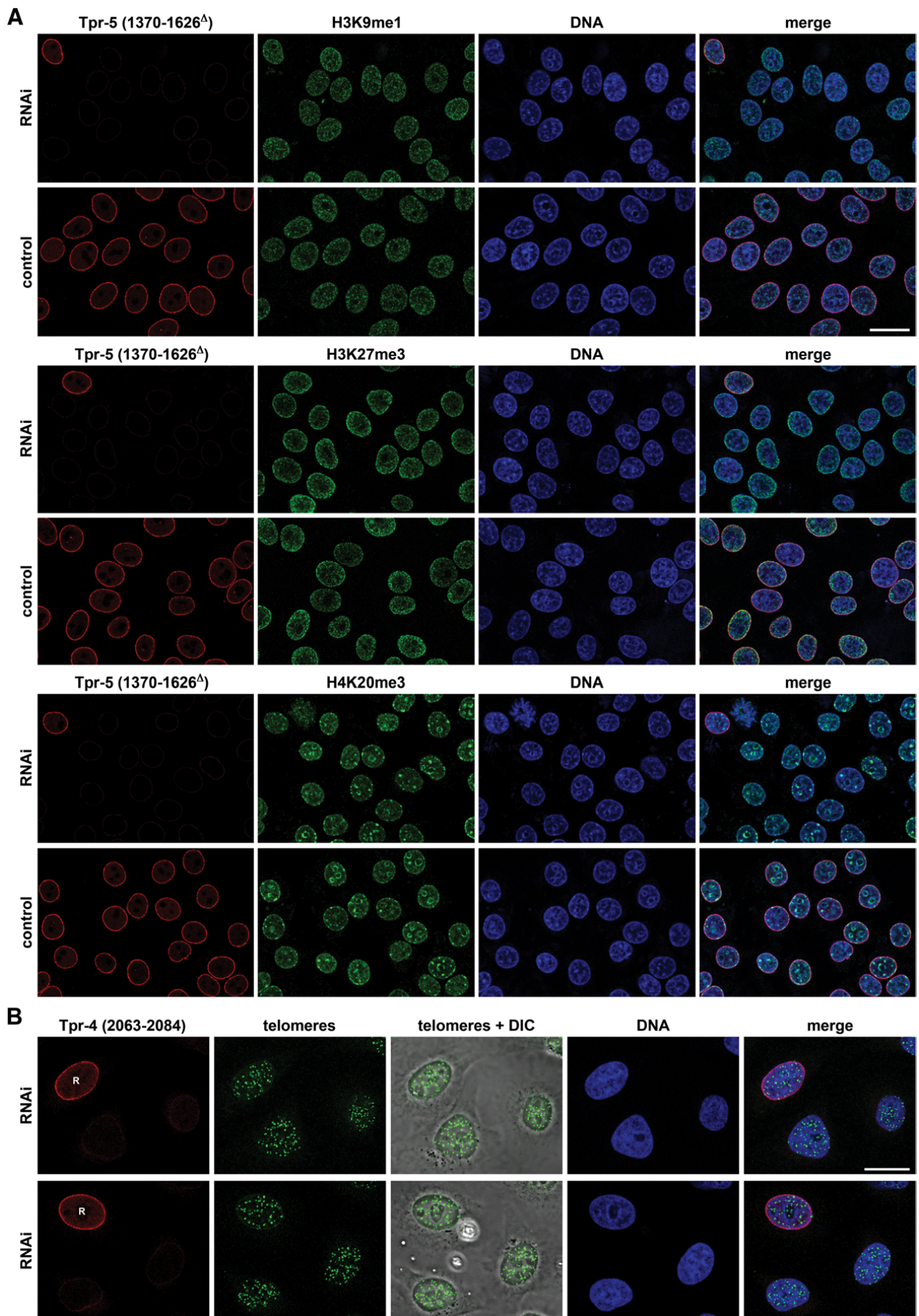- Zinc fingers
- NPC binding domain

B

Supplementary Figure S3. Most NPC core proteins remain largely intact during PV-infection whilst others, including most FG-repeat nucleoporins, are targets of proteolysis. (A) Relative target site positions of antibodies against NPC proteins[S52], except for Nup98. Most antibodies have been described earlier[S43, S53, S54]. Anti-Nup37 (1-326) and anti-Nup214-3 (2076-2090) were provided by Valerie Doye and Ralph Kehlenbach, respectively. Several antibodies targeting the same protein are numbered for clarity. Protein schemes are drawn in scale relative to each other. Schemes for Nup153 and Tpr also include target sites of antibodies not presented in Figure 3. For proteins marked by asterisks not all immunoblot results with different antibodies have been shown in this study. **(B)** Whole protein extracts from the same culture as in Figures 1 and 3 were analysed by immunoblotting. At 8-12 h pi, when NPC-associated HEZs are visible at almost all NPCs, the FG-repeat domains of Nup358, Nup214, Pom121, Nup62, Nup58 and Nup54, but not of CG1 and Nup50, are largely degraded. Similarly, no stable degradation products were observed with mAb414 (not shown) that binds primarily to the FG-repeats of Nup153 and Nup62, but also to those of other FG-repeat family members[S55]. Moreover, using rat monoclonal antibody R4C8 [Abcam Inc., Cambridge, MA; here named anti-Nup153-5 (610-1191^)] that targets an epitope located between aa 610-1191 of rat Nup153, we could not detect any degradation products. This result though needs to be treated with some caution since the immunoblot signal intensity for the full-length human Nup153 protein was already rather feeble for non-infected HeLa cells and at 2-5 h pi, before being no longer detectable at 8-12 h pi (not shown; for usefulness of this antibody in IFM, see Supplementary Figure S4). Disappearance of the electron-dense NPC-midplane concomitant to proteolysis of nucleoporins indicates that some of these proteins contribute to this NPC core feature. In contrast, the NPC anchor domain of the cytoplasmic Nup358 withstands degradation. Furthermore, the N-terminus of the Nup155-interaction partner Nup35, located within the NPC core, is proteolytically removed. In contrast, most members of the Nup160 and Nup205 subcomplexes, forming the NPC core framework, as well as transmembrane proteins gp210 and NDC1 remain intact. Of the Nup160 subcomplex, only a fraction of the Nup96 polypeptides appears degraded. In case of the Nup205 subcomplex, a reproducible reduction in signal intensity was noted for Nup188 when labelled with antibodies against aa 110-124 (not shown) and aa 500-514. Since we failed to raise antibodies against the N- and C-terminus of Nup188, it remains to be shown whether a stable degradation product of Nup188 persists. Tpr blots similar to those shown in Figure 3 are shown as reference. No degradation products of Tpr's C-terminal tail domain were found with any of the "tail"-reactive Tpr antibodies available. These included peptide antibodies against hsTpr aa 2338-2363 (not shown) and aa 2063-2084, and as well as antibodies against *Xenopus* Tpr polypeptides comprising aa 1603-1800 and aa 2070-2321 (not shown), corresponding to and cross-reactive with hsTpr segments aa 1607-1816 and aa 2102-2363. Open brackets labelled "U" denote antibody cross-reactions unrelated to the respective target proteins. Arrows mark "full-length" Nup58, Nup214, Nup358 and gp210. A certain amount of gp210 (asterisk) sometimes exhibited anomalous mobility in Thomas and Kornberg[S56] gels, the PAGE system used throughout this study. Double asterisks mark a potential variant of Nup214, also recognized by antibodies against Nup214 aa 781-797 (not shown).

A

	Nup	Tpr	DNA	DIC
Nup205 (1785-1804)				
Nup35-2 (143-166)				
gp210 (1871-1887)				
Nup62-2 (510-522)				
POM121-2 (347-368)				
POM121-4 (1204-1226)				
Nup358-2 (2180-2211)				
mAb414				
Nup153-4 (1459-1475)				

B

	Nup	Tpr	DNA	merge
Nup153-5 (610-1191$^\Delta$)				

**Supplementary Figure S4. Nucleoporins forming the NPC core structure remain bound to the NE in PV-infected HeLa cells whilst FG-repeat domains are lost. (A)** HeLa cells were studied by non-confocal IFM at 8-10 h pi. Antibodies against components of the Nup205 subcomplex, represented by Nup205, labelled the NE even at these late time points, similar to the Nup160 subcomplex members shown in Figure 4. The truncated Nup35 polypeptide likewise remained bound to the NPC, as did transmembrane NPC protein gp210. Moreover, the NPC anchor domains of FG-repeat family members, here represented by Nup62 and Pom121, were still detectable in some cells at this time point. In contrast, the FG-repeat domains themselves, here represented by Pom121 and Nup358, were no longer detectable in any of the PV-infected cells. In fact, their nuclei were also no longer stained with mAb414 which binds primarily to the FG-repeats of Nup153 and Nup62[S55]. Typical mAb414-staining of a cell that has escaped PV-infection (arrowhead) is shown for comparison. Nuclear rim-staining of another non-infected cell (arrowhead) with anti-Nup153-4 (1459-1475) is included to demonstrate actual target recognition by this antibody also in IFM, as this has not yet been presented in earlier studies. Cells were studied primarily at 8-10 h instead of 12 h pi because a majority of the cells tended to detach from coverslips due to PV-induced "cell-rounding" at the latter time point. Antibody numbering is according to Figure 3C and Supplementary Figure S3A. Bar, 10 μm, same magnification for all micrographs. **(B)** Confocal IFM of cells labelled with antibodies against the distal end of Tpr's rod domain [anti-Tpr-3 (1622-1640)] and against an epitope located between aa 610-1191 of Nup153 [anti-Nup153-5 (610-1191^)] (see also Supplementary Figure S3). Anti-Tpr-3 (1622-1640) still labelled the NEs of PV-infected cells when no or only traces of residual nuclear rim-staining were seen with anti-Nup153-5 (610-1191^). Typical staining of a cell with anti-Nup153-5 (610-1191^) that has escaped PV-infection (arrowhead) is shown for comparison. Bar, 10 μm.

A

Tpr-5 (1370-1626$^\Delta$)	H3K9me1	DNA	merge

RNAi

control

Tpr-5 (1370-1626$^\Delta$)	H3K27me3	DNA	merge

RNAi

control

Tpr-5 (1370-1626$^\Delta$)	H4K20me3	DNA	merge

RNAi

control

B

| Tpr-4 (2063-2084)	telomeres	telomeres + DIC	DNA	merge

RNAi

RNAi

Supplementary Figure S5. Epigenetic histone modifications and telomere positioning in HeLa cells after Tpr knockdown. Cells were studied by confocal IFM. **(A)** Labelling patterns of certain histone lysine methylation types are similar in asynchronous cultures of Tpr siRNA-transfected cells at day 4 post-transfection and accompanying control cells. Antibodies against histone H3 mono-methylated at lysine 9 (H3K9me1), H3 tri-methylated at lysine 27 (H3K27me3), and H4 tri-methylated at lysine 20 (H4K20me3), reported markers in cultured cells for silenced euchromatin, facultative heterochromatin, and constitutive heterochromatin, respectively[S57, S58], were from Abcam Inc. (Cambridge, MA) or provided by Wolfgang Fischle. Overall staining patterns did not differ markedly between the majority of cells transfected with Tpr siRNAs or non-target siRNAs. Only the proportion of Tpr-deficient cells with a moderately more intense H3K9me1-, H3K27me3- or H4K20me3-staining along the NE or around the nucleoli appeared slightly elevated as compared to the range of staining intensities in the controls. Similar results were obtained for Tpr Ib3- and IV4-transfected cell populations. Bars, 20 μm. **(B)** Patterns of telomere and centromere localization are similar in corresponding cell cycle phases of control cells and the majority of Tpr siRNA-transfected cells at day 4 post-transfection. Telomeres were labelled by *in situ* hybridization to the telomere repeat sequence TTAGGG (DAKO telomere PNA FISH kit, Denmark) in asynchronous (not shown) and synchronized cell populations. When determining the positions of telomeres relative to the NE in near-equatorial optical sections of nuclei with similar diameter and DNA content, the percentage of NE-associated (distance to the NE ≤0.5 μm) telomeres was found to be similar in Tpr-deficient cells (16.7% [SD 2.0%], n=4x350-380 signals) and in neighbouring non-transfected cells (16.5% [SD 2.3%], n=3x360-390 signals). Images presented in (B) are from cultures transfected with Tpr siRNAs described earlier[S59]. Non-transfected cells (R) are shown as reference. Corresponding experiments with Tpr siRNAs IB3 and IV4 yielded similar results and no evidence for telomere mislocalization (not shown). We also found centromeric protein distributions, using α-CENP-B autoimmune antibodies (provided by Christer Höög) and an expression vector encoding Flag-tagged CENP-C to be similar in the majority of control and Tpr-deficient cells (not shown). In fact, only after detailed inspection of different focus planes did we note that some few Tpr-deficient cells contained a higher number of centromere and telomere dot signals per cell, as compared to maximal dot numbers in control cells. Centromere dots then appeared smaller in size and less clustered around the nucleoli but instead more distributed across the nuclear interior. Whether this might reflect additional chromosome segregation defects and further karyotype alterations in a subpopulation of Tpr-deficient cells was not further investigated in this anyhow highly mixoploid cell line. Bar, 20 μm; same magnification for all images.

Supplementary Text to Figure 5. Fate of NPC-associated HEZs in HeLa cells after Tpr knockdown. For analysis by EM, sections of control cells and cells treated with siRNAs had been coded prior to evaluation, including control samples unknown to the analyser. In 40-50 randomly chosen interphase cell sections of each specimen, of all perpendicularly sectioned NPCs later attributed to the different controls (n_{total}=739), only 5.8%-7.3% (n_{total}=48) were covered by heterochromatic or nucleolar material, similar to the results in untreated cells (Supplementary Figure S1A). Most of these NPCs, termed "mantled" in the following, exhibited a distinct HEZ (93.8%, n=45), whilst two (4.1%) appeared somewhat incomplete, and one (2.1%) lacked such a clearance zone. In contrast, of the perpendicularly sectioned NPCs (n_{total}=749) attributed to the different Tpr siRNA-transfected cell populations, the percentages of those mantled by either heterochromatic or nucleolar material were somewhat higher (8.8%-11.3%, n_{total}=75). Most of the mantled NPCs in these cell populations lacked an HEZ (60.7%-68.1%; n_{total}=49) whilst other HEZs appeared incomplete or fragmentary (17.9%-21.3%; n_{total}=15), indicative that Tpr played a role in their establishment or maintenance. However, a considerable percentage of the mantled NPCs were still associated to an intact HEZ (12.8%-21.4%, n_{total}=12). Even though most of these HEZs, in terms of figures, could be attributed to the proportion of cells that had remained non-transfected, their total quota somewhat exceeded the percentage of the residual Tpr protein content in Tpr siRNA-transfected populations analyzed by immunoblotting. At this point of our studies, we conceived different explanations for these findings. (i) First, we did not know whether the appendices of the subgroup of NPCs that were associated to nucleoli or naturally occurring heterochromatin clusters were indeed identical to those assumed to be attached to the majority of other NPCs, where HEZs had been reported to become visible only after PV-infection[S39, S60]. (ii) Secondly, we could also not yet exclude that other NPC proteins such as Nup153, known to remain intact in such Tpr-deficient cells ([S59], Figure 5B) could contribute to HEZ maintenance and be responsible for the subgroup of HEZs that appeared incomplete or fragmentary. (iii) Finally, we could not rule out that residual Tpr polypeptides that became surrounded by heterochromatic or nucleolar material in an interphase cell were temporarily protected from catabolic elimination, i.e. at least for the length of one interphase and in contrast to Tpr polypeptides at other NPCs. In fact, IFM occasionally revealed residual Tpr-positive dots at NEs that otherwise were largely Tpr-depleted (see Supplementary Figure S6). In addition to the findings regarding HEZ fate, TEM further revealed that NE-attachment of the nucleolus in G1-phase, and that of the rare large clusters of heterochromatic material in Tpr siRNA-treated cells remained unaffected by Tpr-deficiency at day 4 post-transfection. However, apart from such sporadic heterochromatin clusters, the thin layer of heterochromatic material typically seen attached between NPCs in late S- and G2-phase[S41, S61] often appeared less electron-dense in the Tpr siRNA-transfected cells than in the controls. Whether Tpr might play some role in establishing or maintaining a certain condensation status of the perinuclear heterochromatin in mid- to late interphase remains to be investigated. Likewise, it is of interest how altered chromatin appearance in TEM can be reconciled with IFM data showing no decrease in the labelling intensity for H3K9me1, H3K27me3 and H4K20me3 modifications at the nuclear periphery of Tpr-deficient cells.

A — Tpr-5 (1370-1626^Δ) | Nup358-2 (2180-2211) | DNA | merge | control

B1, **B2**, **B3**, **B4**, **B5** — Tpr RNAi
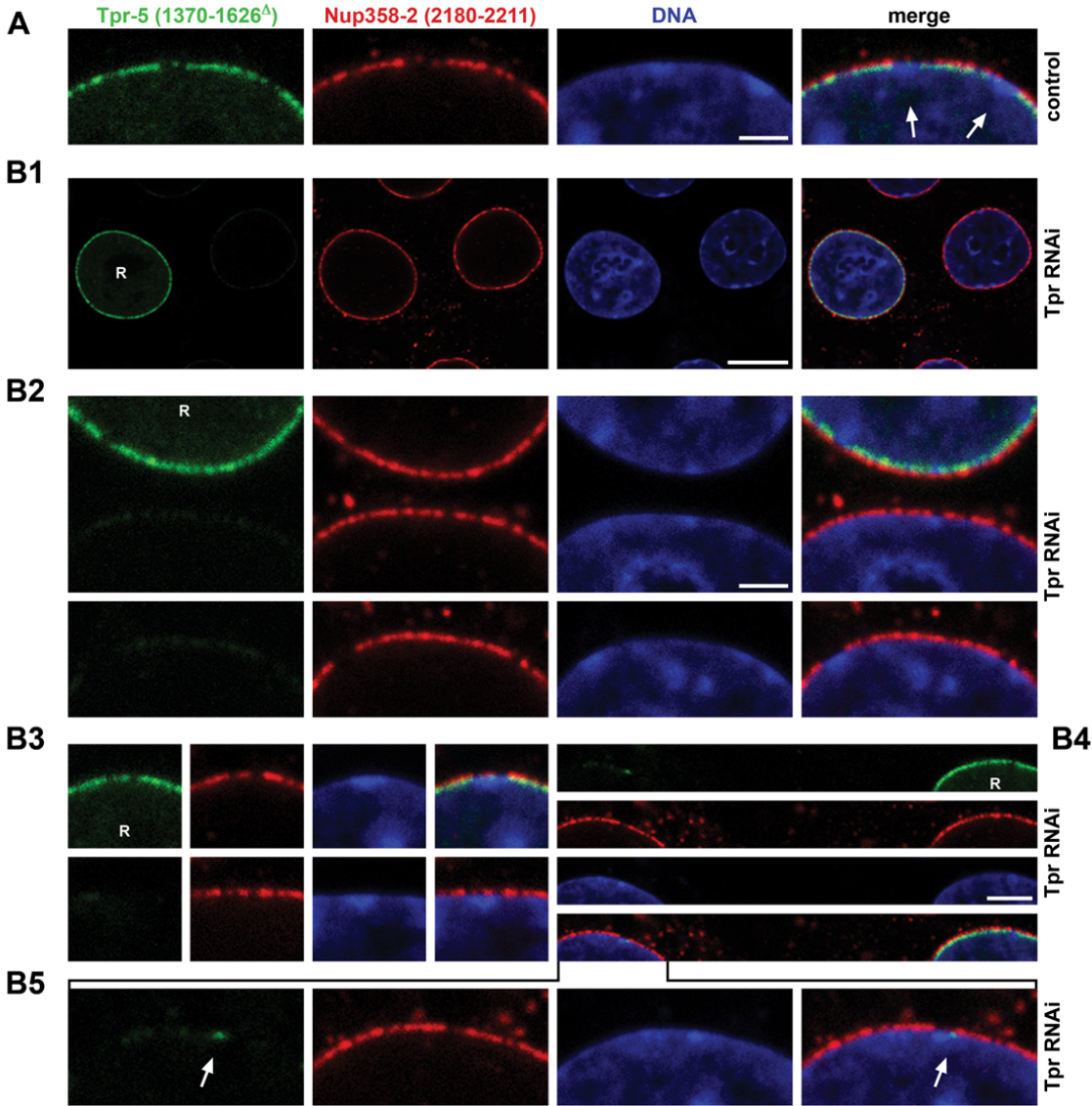
Supplementary Figure S6. Fate of a subpopulation of NPC-associated Tpr polypetides in HeLa cells after Tpr knockdown. Confocal IFM of dot-like remnants of Tpr staining at the NE of cells at day 4 post-transfection with Tpr siRNAs. **(A)** Non-transfected reference cell, double-labelled with antibodies against Tpr (1370-1626[A]) and cytoplasmic Nup358 (2180-2211). In general, Nup358 and Tpr signals were found adjacent to each other all along the NE, only locally gapped by apparently pore-less regions (right arrow). Such gaps were often placed above patches of more brightly stained chromatin. Assuming that the patches represent heterochromatic material, these observations would be in line with former findings of sparse NPC occurrence in contact regions between NE and heterochromatin clusters[S2]. However, small chromatin clusters placed beneath NE segments with seemingly normal NPC frequency (not shown) or "decorated" by single pores (left arrow) were also seen. **(B1-B5)** Tpr siRNA-transfected cells and neighbouring non-transfected cells shown as reference (R). Whilst Tpr staining was often diminished rather uniformly along the NEs of most cells (B1, B2), and also at NPCs positioned next to chromatin clusters (B3), dot-like islands of more intense residual Tpr staining (arrow) were occasionally observed as well (B4, B5). This suggests that individual groups of Tpr polypeptides sometimes withstood elimination longer. B4 demonstrates identical microscope settings for the recording of the Tpr siRNA-transfected cell shown in B5 and a neighbouring non-transfected one. Dot-like Nup358-staining in the cytoplasmic compartment represents NPC-containing annulate lamellae that contain proteins of the NPC core and its cytoplasmic appendices[S62] but are devoid of Tpr[S63]. Bars, 2 μm (A, B2), 10 μm (B1), 4 μm (B4); same magnification for micrographs in B2, B3 and B5.

A

B
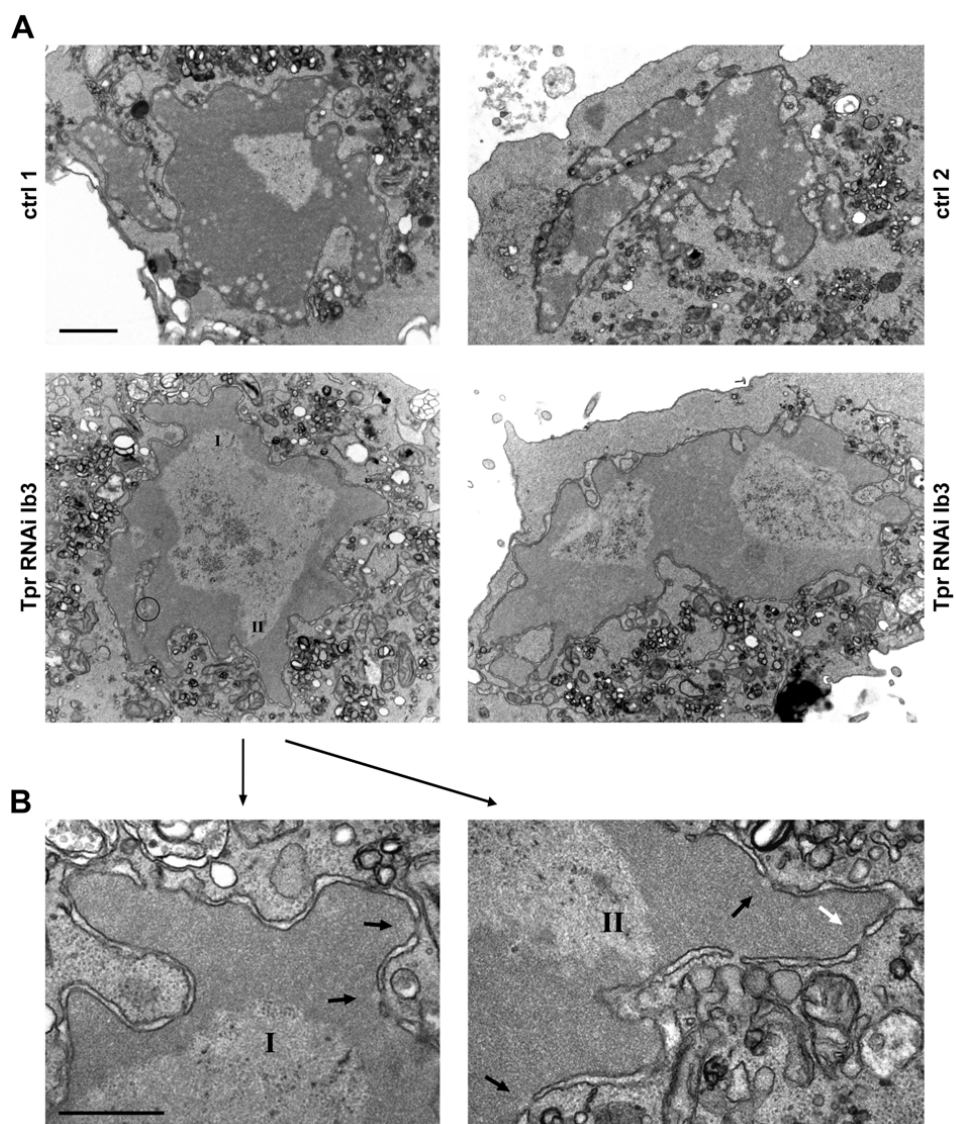
Supplementary Figure S7. Overview micrographs illustrate absence and presence of NPC-associated HEZs in Tpr siRNA-transfected and control cells after subsequent PV-infection. (A) Upper row: TEM overviews of mock-transfected HeLa cells, PV-infected at day 4 post-transfection and harvested 9.5-10 h later. The majority of NPCs possess HEZs contoured but not trespassed by the hyper-condensed chromatin masses. Lower row: HeLa cells were Tpr siRNA-transfected, PV-infected, and harvested 9.5-10 h later, in parallel to specimens shown in the upper row. The nuclear entrances of almost all NPCs are devoid of HEZs and coated by hyper-condensed chromatin. A possible HEZ in the left image is encircled. Such occasionally observed residual HEZs might correspond to the residual Tpr NE-signals of dot-like appearance sometimes seen by IFM (Supplementary Figure S6). Areas marked I and II in the left image are shown in higher magnification in (B). Tpr-RNAi specimens and controls had been coded for analysis. Condensed chromatin in the Tpr siRNA-transfected and then PV-infected cells often appeared less intensely stained by heavy metals than in the controls. Whether this solely reflects a delay in the chromatin compaction process, in keeping with the delay in nucleoporin proteolysis in the Tpr siRNA-transfected cells (Figure 6), or whether it correlates with an altered condensation status of perinuclear chromatin remains to be investigated. Even though PV-induced chromatin compaction remains mechanistically unexplained, its partial similarity to apoptotic chromatin condensation[S64, S65] indicates that dephosphorylation of chromatin-associated proteins might play a major role[S66]. If so, Tpr-deficiency might cause alterations in their phosphorylation states. Bar, 1 μm; same magnification for all images. **(B)** A thin residual band of less electron-dense material of 10-15 nm thickness, seen directly in front of some NPCs (one marked by white arrow) might represent the nuclear ring, a part of the NPC proper known to be of similar thickness[S50, S51], to be poorly stainable by heavy metals under similar conditions of specimen preparation, and to contain some of the Nup107 subcomplex nucleoporins not degraded during PV-infection (Figures 3-5, Supplementary Figure S3). In addition, small, tuft-like appendices of fuzzy appearance were seen at some NPCs (some pointed at by black arrows), most of which still contained an electron-dense midplane or remnants thereof. Since presence of the midplane indicates that the FG-nucleoporins of the corresponding NPC might not yet be completely degraded (Supplementary Figure S3), and since PV-induced degradation of NPC proteins in Tpr-RNAi cells is indeed somewhat decelerated compared to control cells (Figure 6), such tufts might represent still intact copies of Nup153, with its large, highly flexible FG-repeat domain still bound to the NPC. Bar, 500 nm; same magnification for both micrographs.

Supplementary References

S1.   McKeown PC, Shaw PJ (2009) Chromatin: linking structure and function in the nucleolus. *Chromosoma* **118:** 11-23

S2.   Maul GG (1977) The nuclear and the cytoplasmic pore complex: structure, dynamics, distribution, and evolution. *Int Rev Cytol Suppl* 75-186

S3.   Murray B, Davies HG (1979) Three-dimensional reconstruction of the chromatin bodies in the nuclei of mature erythrocytes from the newt Triturus cristatus: the number of nuclear envelope-attachment sites. *J Cell Sci* **35:** 59-66

S4.   Lopez-Velazquez G, Marquez J, Ubaldo E, Corkidi G, Echeverria O, Vazquez Nin GH (1996) Three-dimensional analysis of the arrangement of compact chromatin in the nucleus of G0 rat lymphocytes. *Histochem Cell Biol* **105:** 153–161

S5.   Leger-Silvestre I, Trumtel S, Noaillac-Depeyre J, Gas N (1999) Functional compartmentalization of the nucleus in the budding yeast Saccharomyces cerevisiae. *Chromosoma* **108:** 103-113

S6.   Galy V, Gadal O, Fromont-Racine M, Romano A, Jacquier A, Nehrbass U (2004) Nuclear retention of unspliced mRNAs in yeast is mediated by perinuclear Mlp1. *Cell* **116:** 63-73

S7.   Benichou JC, Quiviger B, Ryter A (1983) Cytochemical study of the nucleolus of the slime mold Dictyostelium discoideum. *J Ultrastruct Res* **84:** 60-66

S8.   Tresse E, Kosta A, Luciani MF, Golstein P (2007) From autophagic to necrotic cell death in Dictyostelium. *Semin Cancer Biol* **17:** 94-100

S9.   Nikolova V, Leimena C, McMahon AC, Tan JC, Chandar S, Jogia D, Kesteven SH, Michalicek J, Otway R, Verheyen F, Rainer S, Stewart CL, Martin D, Feneley MP, Fatkin D (2004) Defects in nuclear structure and function promote dilated cardiomyopathy in lamin A/C-deficient mice. *J Clin Invest* **113:** 357-369

S10.   Shultz LD, Lyons BL, Burzenski LM, Gott B, Samuels R, Schweitzer PA, Dreger C, Herrmann H, Kalscheuer V, Olins AL, Olins DE, Sperling K, Hoffmann K (2003) Mutations at the mouse ichthyosis locus are within the lamin B receptor gene: a single gene model for human Pelger-Huet anomaly. *Hum Mol Genet* **12:** 61-69

S11.   Cronshaw JM, Matunis MJ (2003) The nuclear pore complex protein ALADIN is mislocalized in triple A syndrome. *Proc Natl Acad Sci U S A* **100:** 5823-5827

S12.   Hirano M, Furiya Y, Asai H, Yasui A, Ueno S (2006) ALADINI482S causes selective failure of nuclear protein import and hypersensitivity to oxidative stress in triple A syndrome. *Proc Natl Acad Sci U S A* **103:** 2298-2303

S13.   Yamazumi Y, Kamiya A, Nishida A, Nishihara A, Iemura S, Natsume T, Akiyama T (2009) The transmembrane nucleoporin NDC1 is required for targeting of ALADIN to nuclear pore complexes. *Biochem Biophys Res Commun* **389:** 100-104

S14.   Kind B, Koehler K, Lorenz M, Huebner A (2009) The nuclear pore complex protein ALADIN is anchored via NDC1 but not via POM121 and GP210 in the nuclear envelope. *Biochem Biophys Res* **390:** 205-210

S15.   Huebner A, Mann P, Rohde E, Kaindl AM, Witt M, Verkade P, Jakubiczka S, Menschikowski M, Stoltenburg-Didinger G, Koehler K (2006) Mice lacking the nuclear pore complex protein ALADIN show female infertility but fail to develop a phenotype resembling human triple A syndrome. *Mol Cell Biol* **26:** 1879-1887

S16.   Swift H (1959) Studies on nuclear fine structure. *Brookhaven Symp Biol* **12:** 134-152

S17.   Watson ML (1959) Further observations on the nuclear envelope of the animal cell. *J Biophys Biochem Cytol* **6:** 147-156

S18.   Davies HG (1961) Structure in nucleated erythrocytes. *J Biophys Biochem Cytol* **9:** 671-687

S19.   Tokuyasu K, Madden SC, Zeldis LJ (1968) Fine structural alterations of interphase nuclei of lymphocytes stimulated to growth activity in vitro. *J Cell Biol* **39:** 630-660

S20.   Monneron A, Blobel G, Palade GE (1972) Fractionation of the nucleus by divalent cations. Isolation of nuclear membranes. *J Cell Biol* **55:** 104-125

S21.   Davies HG, Murray AB, Walmsley ME (1974) Electron-microscope observations on the organization of the nucleus in chicken erythrocytes and a superunit thread hypothesis for chromosome structure. *J Cell Sci* **16:** 261-299

S22.   Lawrence IEJ, Burden HW, Capps ML (1977) Ultrastructure of rat ovarian interstitial gland cells during pregnancy. *Cell Tissue Res* **184:** 143-154

S23.   Nakano M, Yamanaka K, Hasegawa A, Sawamura R, Okada S (1992) Preferential increase of heterochromatin in venular endothelium of lung in mice after administration of dimethylarsinic acid, a major metabolite of inorganic arsenics. *Carcinogenesis* **13:** 391-393

S24.   Knop E, Reale E (1994) Fine structure and significance of snakelike chromatin in conjunctival

epithelial cells. *Invest Ophthalmol Vis Sci* **35:** 711-719

S25. Faria AMC, Levay A, Wang Y, Kamphorst AO, Rosa MLP, Nussenzveig DR, Balkan W, Chook YM, Levy DE, Fontoura BMA (2006) The nucleoporin Nup96 is required for proper expression of interferon-regulated proteins and functions. *Immunity* **24:** 295-304

S26. La Pushin RW, de Harven E (1971) A study of gluco-corticosteroid-induced pyknosis in the thymus and lymph node of the adrenalectomized rat. *J Cell Biol* **50:** 583-597

S27. Tani E, Ametani T, Higashi N, Fujihara E (1972) Nuclear periphery of human glioma and meningioma cells. *Acta Neuropathol* **20:** 32-42

S28. Costello C, Catovsky D, O'Brien M, Galton DA (1980) Prolymphocytic leukaemia: an ultrastructural study of 22 cases. *Br J Haematol* **44:** 389-394

S29. Jakobiec FA (1984) The ultrastructure of conjunctival melanocytic tumors. *Trans Am Ophthalmol Soc* **82:** 599-752

S30. Ghadially FN, Senoo A, Fuse Y (1985) A serial section study of nuclear pockets containing nuclear material. *J Submicrosc Cytol* **17:** 687-694

S31. Sewry CA, Brown SC, Mercuri E, Bonne G, Feng L, Camici G, Morris GE, Muntoni F (2001) Skeletal muscle pathology in autosomal dominant Emery-Dreifuss muscular dystrophy with lamin A/C mutations. *Neuropathol Appl Neurobiol* **27:** 281-290

S32. Visser AE, Jaunin F, Fakan S, Aten JA (2000) High resolution analysis of interphase chromosome domains. *J Cell Sci* **113:** 2585-2593

S33. Rego A, Sinclair PB, Tao W, Kireev I, Belmont AS (2008) The facultative heterochromatin of the inactive X chromosome has a distinctive condensed ultrastructure. *J Cell Sci* **121:** 1119-1127

S34. Franke WW, Scheer U (1974) Structures and functions of the nuclear envelope. In *The Cell Nucleus*, Busch H (ed) pp 219-347. New York: Academic Press Inc.

S35. Scheer U, Dabauvalle MC, Merkert H, Benevente R (1988) The nuclear envelope and the organization of the pore complexes. *Cell Biol Int Rep* **12:** 669-689

S36. Ris H (1997) High-resolution field-emission scanning electron microscopy of nuclear pore complex. *Scanning* **19:** 368-375

S37. Gruzova MN, Parfenov VN (1977) Ultrastructure of late oocyte nuclei in Rana temporaria. *J Cell Sci* **28:** 1-13

S38. Gustin KE, Sarnow P (2001) Effects of poliovirus infection on nucleo-cytoplasmic trafficking and nuclear pore complex composition. *EMBO J* **20:** 240-249

S39. Belov GA, Lidsky PV, Mikitas OV, Egger D, Lukyanov KA, Bienz K, Agol VI (2004) Bidirectional increase in permeability of nuclear envelope upon poliovirus infection and accompanying alterations of nuclear pores. *J Virol* **78:** 10166-10177

S40. Park N, Katikaneni P, Skern T, Gustin KE (2008) Differential targeting of nuclear pore complex proteins in poliovirus-infected cells. *J Virol* **82:** 1647-1655

S41. Erlandson RA, de Harven E (1971) The ultrastructure of synchronized HeLa cells. *J Cell Sci* **8:** 353-397

S42. Hawes P, Netherton CL, Mueller M, Wileman T, Monaghan P (2007) Rapid freeze-substitution preserves membranes in high-pressure frozen tissue culture cells. *J Microsc* **226:** 182-189

S43. Krull S, Thyberg J, Björkroth B, Rackwitz HR, Cordes VC (2004) Nucleoporins as components of the nuclear pore complex core structure and Tpr as the architectural element of the nuclear basket. *Mol Biol Cell* **15:** 4261-4277

S44. Weibel ER, Kistler GS, Scherle WF (1966) Practical stereological methods for morphometric cytology. *J Cell Biol* **30:** 23-38

S45. Weibel ER (1969) Stereological principles for morphometry in electron microscopic cytology. *Int Rev Cytol* **26:** 235-302

S46. Sakai T (1980) Relation between thickness and interference colors of biological ultrathin section. *J Electron Micros* **29:** 369-375

S47. De Groot DMG (1988) Comparison of methods for the estimation of the thickness of ultrathin tissue sections. *J Micros* **151:** 23-42

S48. Richardson WD, Davies HG (1980) Quantitative observations on the kinetics and mechanisms of binding of electron stains to thin sections through hen erythrocytes. *J Cell Sci* **46:** 253-278

S49. Cattini PA, Davies HG (1983) Kinetics of lead citrate staining of thin sections for electron microscopy. *Stain Technol* **58:** 29-40

S50. Akey CW, Radermacher M (1993) Architecture of the Xenopus nuclear pore complex revealed by three-dimensional cryo-electron microscopy. *J Cell Biol* **122:** 1-19

S51. Hinshaw JE, Carragher BO, Milligan RA (1992) Architecture and design of the nuclear pore complex. *Cell* **69:** 1133-1141

S52. Cronshaw JM, Krutchinsky AN, Zhang W, Chait BT, Matunis MJ (2002) Proteomic analysis of the

mammalian nuclear pore complex. *J Cell Biol* **158:** 915-927

S53.   Patre M, Tabbert A, Hermann D, Walczak H, Rackwitz HR, Cordes VC, Ferrando-May E (2006) Caspases target only two architectural components within the core structure of the nuclear pore complex. *J Biol Chem* **281:** 1296-1304

S54.   Stavru F, Hülsmann BB, Spang A, Hartmann E, Cordes VC, Görlich D (2006) NDC1: a crucial membrane-integral nucleoporin of metazoan nuclear pore complexes. *J Cell Biol* **173:** 509-519

S55.   Sukegawa J, Blobel G (1993) A nuclear pore complex protein that contains zinc finger motifs, binds DNA, and faces the nucleoplasm. *Cell* **72:** 29-38

S56.   Thomas JO, Kornberg RD (1975) An octamer of histones in chromatin and free in solution. *Proc Natl Acad Sci U S A* **72:** 2626-2630

S57.   Bartova E, Krejci J, Harnicarova A, Galiova G, Kozubek S (2008) Histone modifications and nuclear architecture: a review. *J Histochem Cytochem* **56:** 711-721

S58.   Zinner R, Albiez H, Walter J, Peters AH, Cremer T, Cremer M (2006) Histone lysine methylation patterns in human cell types are arranged in distinct three-dimensional nuclear zones. *Histochem Cell Biol* **125:** 3-19

S59.   Hase ME, Cordes VC (2003) Direct interaction with Nup153 mediates binding of Tpr to the periphery of the nuclear pore complex. *Mol Biol Cell* **14:** 1923-1940

S60.   Bienz K, Egger D, Wolff DA (1973) Virus replication, cytopathology, and lysosomal enzyme response of mitotic and interphase Hep-2 cells infected with poliovirus. *J Virol* **11:** 565-574

S61.   Setterfield G, Sheinin R, Dardick I, Kiss G, Dubsky M (1978) Structure of interphase nuclei in relation to the cell cycle. Chromatin organization in mouse L cells temperature-sensitive for DNA replication. *J Cell Biol* **77:** 246-263

S62.   Cordes VC, Reidenbach S, Franke WW (1996) Cytoplasmic annulate lamellae in cultured cells: composition, distribution, and mitotic behavior. *Cell Tissue Res* **284:** 177-191

S63.   Cordes VC, Reidenbach S, Rackwitz HR, Franke WW (1997) Identification of protein p270/Tpr as a constitutive component of the nuclear pore complex-attached intranuclear filaments. *J Cell Biol* **136:** 515-529

S64.   Agol VI, Belov GA, Bienz K, Egger D, Kolesnikova MS, Raikhlin NT, Romanova LI, Smirnova EA, Tolskaya EA (1998) Two types of death of poliovirus-infected cells: caspase involvement in the apoptosis but not cytopathic effect. *Virology* **252:** 343-353

S65.   Agol VI, Belov GA, Bienz K, Egger D, Kolesnikova MS, Romanova LI, Sladkova LV, Tolskaya EA (2000) Competing death programs in poliovirus-infected cells: commitment switch in the middle of the infectious cycle. *J Virol* **74:** 5534-5541

S66.   Lu Z, Zhang C, Zhai Z (2005) Nucleoplasmin regulates chromatin condensation during apoptosis. *Proc Natl Acad Sci U S A* **102:** 2778-2783